

Phase Aberration Correction: A Deep Learning-Based Aberration to Aberration Approach

Mostafa Sharifzadeh, Sobhan Goudarzi, An Tang, Habib Benali, *Fellow, IEEE*,
and Hassan Rivaz, *Senior Member, IEEE*

Abstract—One of the primary sources of suboptimal image quality in ultrasound imaging is phase aberration. It is caused by spatial changes in sound speed over a heterogeneous medium, which disturbs the transmitted waves and prevents coherent summation of echo signals. Obtaining non-aberrated ground truths in real-world scenarios can be extremely challenging, if not impossible. This challenge hinders training of deep learning-based techniques' performance due to the presence of domain shift between simulated and experimental data. Here, for the first time, we propose a deep learning-based method that does not require ground truth to correct the phase aberration problem, and as such, can be directly trained on real data. We train a network wherein both the input and target output are randomly aberrated radio frequency (RF) data. Moreover, we demonstrate that a conventional loss function such as mean square error is inadequate for training such a network to achieve optimal performance. Instead, we propose an adaptive mixed loss function that employs both B-mode and RF data, resulting in more efficient convergence and enhanced performance. Finally, we publicly release our dataset, including 161,701 single plane-wave images (RF data). This dataset serves to mitigate the data scarcity problem in the development of deep learning-based techniques for phase aberration correction. Source code and trained model will be released along with the dataset at <http://code.sonography.ai/pac-aaa>.

Index Terms—phase aberration, ultrasound imaging, adaptive mixed loss, neural networks.

I. INTRODUCTION

Ultrasound imaging is commonly used for medical diagnosis and image-guided interventions [1] due to its advantages, such as portability, non-invasiveness, high temporal resolution, and low cost. However, it often suffers from artifacts, with phase aberration as one of the main sources of image quality degradation [2].

Spatially varying sound speed while traveling through a heterogeneous medium is the origin of the phase aberration effect [3]. In a perfect homogeneous medium, where the sound speed is constant and known, the traveling time for a pulse from any transducer element to any point in the medium can be calculated using simple geometry. Therefore, the required time delays that need to be applied to each element can be determined accurately to compensate for traveling path length differences and form the desired beam in transmit beamforming. Similarly, in receive beamforming, time delays

can be calculated and applied to received echo signals in order to sum them coherently. In practice, however, the human body is a heterogeneous medium, where, for instance, the sound speed in fat and muscle is approximately 1460 m/s and 1610 m/s, respectively, which indicates a variation of almost 10% [4]. The variation is even higher in applications such as transcranial imaging [5], where the sound speed in the skull is nearly 2740 m/s [6]. The phase aberration effect in a heterogeneous medium alters the focal point in focused imaging and perturbs the flat wavefront propagation in plane-wave imaging during the transmission, and prevents coherent summation of echo signals in both imaging techniques during the reception, all of which cause suboptimal image quality.

A. Related Work

Aberration correction has been studied for years in the medical ultrasound community, as it can improve anatomical fidelity and spatial localization, both of which lead to improved diagnostic accuracy and precision of image-guided interventions. Several techniques attempted to estimate delay errors by maximizing the cross-correlation [3] or minimizing the absolute differences between RF signals received at adjacent array elements [7], maximizing mean speckle brightness in a region of interest [8], or incorporating a virtual point reflector generated by iterative time reversal focusing [9]. Li *et al.* utilized the generalized coherence factor for reducing focusing errors, especially the ones caused by sound speed inhomogeneities [10]. Napolitano *et al.* analyzed lateral spatial frequency content in reconstructed images to find the optimal sound speed for subsequent imaging that maximizes the focus quality [11]. Shin *et al.* employed an adaptive filtering technique called frequency-space prediction filtering (FXPF), which presupposes the existence of an autoregressive model across the echo signals received at the transducer elements and removes any components that do not conform to the established model [12], [13].

As opposed to methods that model the phase aberration effect by a fixed near-field phase screen in front of the transducer, the locally adaptive phase aberration correction technique [14] assumed a spatially varying near-field phase screen and employed multistatic synthetic aperture data to perform the correction at each point adaptively. Lambert *et al.* suggested compensating for the spatially-distributed aberrations by decoupling aberrations undergone by the outgoing and incoming waves utilizing the distortion matrix built from the focused reflection matrix, which contains the responses

M. Sharifzadeh, H. Benali, and H. Rivaz are with the Department of Electrical and Computer Engineering, Concordia University, Montreal, QC, Canada. S. Goudarzi is with the Physical Science Platform, Sunnybrook Research Institute, Toronto, ON, Canada. A. Tang is with the Department of Radiology, Radiation Oncology and Nuclear Medicine, Université de Montréal, Montreal, QC, Canada.

between virtual transducers synthesized from the transmitted and received focal spots [15], [16], [17].

A different category of techniques utilizes echo signals as input and returns an estimation of the spatial distribution of sound speed in a given medium [18], [19]. Although these methods are not an immediate approach for aberration correction, the estimated distribution can be subsequently employed to compensate for the phase aberration effect, for instance, by reconstructing the image by computing beamforming delays assuming that sound travels on straight line paths [20] or using a set of refraction-corrected delays based on the Eikonal equation [21], which can be efficiently solved using the fast marching method [22]. The computed ultrasound tomography in echo mode (CUTE) method correlated the phase shifts across a sequence of beamformed plane-wave images obtained with different steering angles and exploited that to estimate the distribution of sound speed [23]. Jakovljevic *et al.* proposed and solved a model via gradient descent that establishes a connection between the local speed of sound along a wave propagation path and the average speed of sound over that path [24], where the latter is measured using the method proposed in [25]. Although the efficacy of this model was demonstrated in layered heterogeneous media, the performance often drops when the variations of sound speed are not insignificant along the lateral axis. Rehman *et al.* introduced a tomography-based method that directly accounts for propagation paths between the scattering volume and each transducer element to mitigate that issue [26]. They also proposed an inverse-modeled phase aberration computed tomography (IMPACT) framework, which utilizes multistatic synthetic aperture data, estimates the global average sound speed [27] by maximizing coherence for each point, applies an inversion to compute the local sound speed, and finally exploits them in two different Eikonal equation-based and wavefield correlation-based distributed aberration correction techniques [28]. In addition to approaches that aim to rectify the aberrated image, beamformers exist which are designed to be robust to this artifact by incorporating singular value decomposition of a defined matrix comprising backscattered data for multiple plane-wave transmissions [29].

Recently, utilizing deep learning (DL)-based techniques for phase aberration correction has attracted growing interest. Among one of the first endeavors, Sharifzadeh *et al.* assumed a near-field phase screen model and demonstrated that a convolutional neural network (CNN) could estimate delay errors, or the aberration profile, directly from the B-mode image with a high accuracy [30]. Feigin *et al.* simulated a dataset using the k-Wave toolbox, wherein the organs in tissue were modeled as uniform ellipses over a homogeneous background with different sound speeds. They trained a CNN on the dataset to estimate sound speed distribution, taking raw RF channel data of three plane-wave transmissions as inputs [31]. In a similar approach, demodulated in-phase and quadrature (IQ) data were provided to the network as the inputs [32]. Additional comparable methodologies have been proposed in the literature [33], [34] for the same purpose. Koike *et al.* trained a network by mapping aberrated RF inputs to their corresponding aberration-free RF target outputs [35]. Shen

et al. utilized a CNN to estimate the aberrated point spread function from beamformed IQ data and subsequently applied the inverse filter to rectify the data [36]. Additionally, there are DL-based beamformers designed to exhibit robustness to the aberration by suppressing off-axis scattering [37] or by mapping images beamformed with randomly perturbed sound speed values to clean images beamformed with a reference sound speed value [38].

B. Contributions

The main challenge in utilizing DL-based approaches for correcting phase aberration is the absence of a reliable ground truth. As a result, the aforementioned methods had to rely solely on simulated data for training, leading to a drop in performance when testing on experimental data due to the domain shift problem. Recent studies have recognized the need to eliminate the requirement of ground truths; however, even in such efforts, reconstructed images with a fixed sound speed value of 1540 m/s were still considered clean images [38]. Our contributions can be summarized as follows:

- 1) We propose the first DL-based aberration correction method that eliminates the need for ground truth in the training phase. Both input and target output are randomly aberrated RF data, which enables us to use real experimental data for training, fine-tuning, or both, without any explicit assumption regarding the presence or absence of phase aberrations.
- 2) Our training setup presents a significant challenge as both the input and desired output of the network contain aberrations that randomly differ in each frame and epoch. Adding to the complexity is the fact that RF data includes high-frequency components. We demonstrate that a conventional loss function such as mean square error (MSE) is inadequate for training such a network. To address this challenge, we introduce a loss function that incorporates both B-mode and RF data and evaluate its performance.
- 3) We will publicly release a dataset consisting of 1,601 single plane-wave image sets (RF data). Each set consists of 100 aberrated versions of the same realization, as well as the non-aberrated version (the non-aberrated version is not used for training in this paper and is provided solely for comprehensiveness). To the best of our knowledge, this is the first dataset that is practically suitable for developing DL-based techniques in this domain, given its size and structure.
- 4) We will release our code and trained model online. Additionally due to the unavailability of a publicly available implementation of the FXPF method, which is compared with the proposed method, we will make our own implementation publicly accessible.

We call our proposed **phase aberration correction** method, which relies on an **aberration-to-aberration** approach, PAC-AAA. We show that PAC-AAA substantially improves aberrated images in simulation and phantom experiments. As one of the authors (AT) is a radiologist, we were also able to visually corroborate improvements in an *in-vivo* image.

II. METHODOLOGY

A. Phase Aberration Model

We modeled the phase aberration effect by assuming a near-field phase screen in front of the transducer, which introduces different delay errors to each transducer element during both transmission and reception. Although this model does not make any assumptions regarding the spatial distribution of sound speed within the medium, it proves particularly useful in scenarios where an aberrator layer in front of the transducer is so dominant that other sources of aberration in the remainder of the medium are negligible. Examples include transcranial imaging, where the skull acts as a potent aberrator [40], and imaging overweight subjects, where the wave must propagate through a thick layer of fat found in the near-field [13]. In both cases, slight lateral variations in the thickness of the strong aberrator layer may impose strong aberrations, often impeding the optimal performance of methods designed to estimate the distribution of sound speed [26].

The aberration profile in this model is represented as an array, where each element of the array corresponds to a delay error value assigned to a specific transducer element. Aberration profiles are characterized by their strength and correlation length. The strength is defined as its root mean square amplitude in nanoseconds, and the correlation length, which represents the spatial frequency content, is defined as the full width at half maximum of its autocorrelation in millimeters [41]. An aberration profile becomes stronger and induces more degradation effect as its strength is increased, and its correlation length is decreased, which means higher amplitude with more fluctuation across the aperture [30]. Experiments were conducted in some literature to estimate the parameters of aberration profiles. For instance, the strength and correlation length for *in-vivo* and *ex-vivo* breast tissue are reported as 28.0 ns, 3.48 mm, and 66.8 ns, 4.3 mm respectively [42], [43]. We generated random aberration profiles by convolving a Gaussian function with Gaussian random numbers [41], where they were varied uniformly in strength and correlation length ranging from 20 to 80 ns, and from 4 to 9 mm, respectively, to encompass a broad range of tissues.

B. Phase Aberration Implementation

We first explain the methodology used for introducing phase aberration into simulated and experimental phantom data. Details regarding the simulation or acquisition of data, as well as where each approach was employed, will be discussed later. The Supplementary Video also provides an overview.

1) *Simulated Aberration*: To introduce the aberration effect into simulated data, we utilized full synthetic aperture data and synthesized aberrated plane-wave images under linear and steady conditions. Fig. 1 demonstrates a typical configuration of ultrasonic imaging systems in the (a) absence and (b) presence of a near-field phase aberrator. A linear array transducer consisting of N elements is positioned in direct contact with the imaging medium of interest. The array is oriented such that the x -axis is parallel to its length, while the depth direction within the imaging medium is represented by the z -axis. After a single plane-wave transmission, the received echo signal at

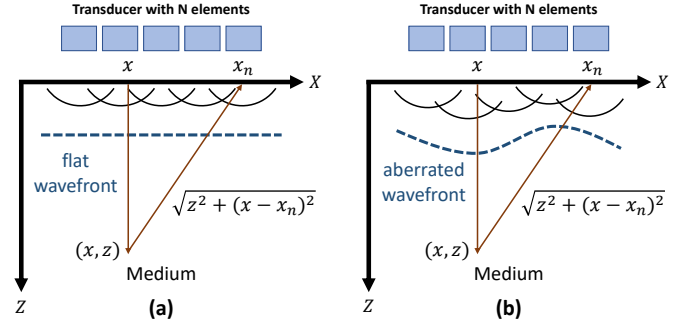


Fig. 1. A typical configuration of ultrasonic imaging systems in the (a) absence and (b) presence of a near-field phase aberrator.

time t by element n located at x_n can be calculated using full synthetic aperture data as follows:

$$RF(x_n, t) = \sum_{m=1}^N RF_{f_{sa}}(x_m, x_n, t + \tau_a(x_m)), \quad (1)$$

where $RF_{f_{sa}}(x_m, x_n, t)$ is the received echo signal at time t by element n located at x_n solely due to excitation of element m located at x_m and $\tau_a(x_m)$ is the delay error that element m experiences according to the aberration profile. In the absence of aberration, as shown in Fig. 1(a), we can assume synchronous excitation times for all piezoelectric elements during synthesizing, equivalent to transmitting a flat wavefront. In this case, the delay error τ_a equals zero for all transducer elements. However, to simulate the phase aberration effect during transmission, as shown in Fig. 1(b), we assumed asynchronous excitation times for piezoelectric elements by applying delay errors imposed by the aberration profile. In the absence of phase aberration, the required time for the acoustic wave to travel to point (x, z) and return to the transducer element n located at x_n is

$$\tau(x_n, x, z) = (z + \sqrt{z^2 + (x - x_n)^2})/c, \quad (2)$$

where c is the sound speed. The phase aberration effect in reception was implemented as a set of disordered delay times corresponding to backscattered signals. To this end, and given the calculated time delay, each point (x, z) within the region of interest can be reconstructed as

$$s(x, z) = \sum_{n=k-[a/2]}^{k+[a/2]} RF(x_n, \tau(x_n, x, z) + \tau_a(x_n)), \quad (3)$$

where k is the nearest transducer element to x , and $[\cdot]$ represents rounding to the nearest integer. Aperture size a determines the number of elements that contribute to the signal and can be expressed using the F-number, which was set to 1.75 in this study and is defined as $F = z/a$. In summary, delay errors $\tau_a(x_m)$ and $\tau_a(x_n)$ in equations (1) and (3) contribute to the aberrations that occur during transmission and reception, respectively, where the former simulates asynchronous excitation of piezoelectric elements during synthesizing the plane-wave and the latter disorders time delays corresponding to received echo signals.

2) *Quasi-physical Aberration*: Our approach for introducing a quasi-physical aberration to an experimental phantom required programming a Vantage 256 research scanner. We programmed the scanner to excite transducer elements asynchronously according to a given aberration profile. To this end, delay errors corresponding to each element were calculated in wavelengths of the transducer center frequency and written to the $TX.Delay$ array, provided by the scanner programming interface. resulting in the generation of an aberrated wavefront during single plane-wave imaging. Moreover, delay errors introduced by the aberration profile were taken into account during the reception process for reconstructing the image.

3) *Physical Aberration*: To introduce a physical aberration to the experimental phantom, we placed an uneven layer of chicken bologna between the probe and the phantom, where the thickness of the left and right halves was approximately 3 mm and 6 mm, respectively. Although the precise value of the sound speed within this layer was unknown, we could be confident that it introduced the aberration effect due to its uneven thickness and observing the effect in the resulting image. To ensure proper contact, we filled the gap between the thinner half and the probe’s surface with conductive gel and positioned the center of the probe at the discontinuity.

C. Datasets

1) *Simulated*: We simulated a synthetic dataset consisting of 160,100 images using the publicly available Field II simulation package [44] containing an average scatterer density of 60 per resolution cell (fully developed speckle pattern) uniformly distributed inside a phantom measuring 45 mm in the lateral and 40 mm in the axial direction and positioned at an axial depth of 10 mm from the face of the transducer. We introduced contrast to the images by incorporating four different types of echogenicities, including anechoic regions, hypoechoic regions, hyperechoic regions, and diverse echogenicities. To generate the first three types, we took 600 samples (200 samples per type) from a publicly available dataset, known as XPIE [45], which included segmented natural images. We then disregarded natural images and resampled only their corresponding segmentation masks to match the phantom’s dimensions. Finally, the amplitude of scatterers located inside the mask was multiplied by a weight, which was zero for anechoic regions, a uniform random number $\in [0.063, 0.501]$ for -12 dB to -3 dB hypoechoic regions, and a uniform random number $\in [2, 15.8]$ for +3 dB to +12 dB hyperechoic regions. To enrich the range of echogenicity, we obtained an additional 1000 samples from the XPIE dataset, but this time we discarded the segmentation masks and instead resampled only the natural images with the same dimensions as the phantom. These images were then converted to grayscale, and similar to [46], the pixel intensities were utilized to weight the scatterers’ amplitude according to their respective positions via bilinear interpolation. To enhance the contrast of the ultrasound images, we preprocessed natural images by performing histogram equalization and thresholding pixel values below 0.1 to zero and those above 0.9 to 1. The image simulation approach described in this subsection offers the advantage of providing

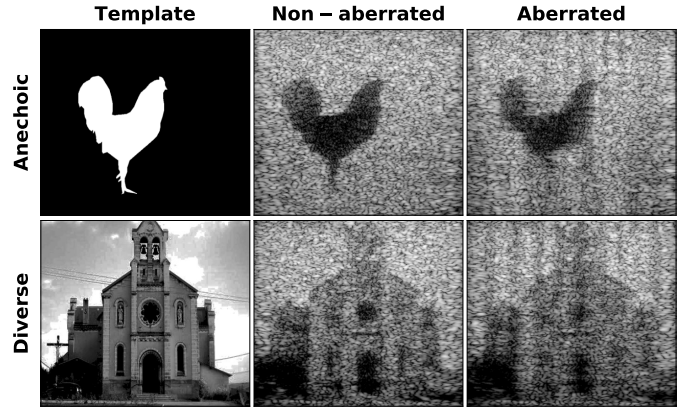


Fig. 2. Samples from the simulated dataset. The first row displays an anechoic region generated using an arbitrary segmentation mask. The second row depicts a diverse echogenicity example generated based on a natural image. For each case, the template, non-aberrated, and a sample aberrated version are presented in the first to third columns, respectively. Templates and non-aberrated images are included solely for visualization purposes and were not utilized in the proposed method.

the network with a broader range of features compared to images containing solely cyst-shaped regions. In addition, one test image comprising two anechoic cysts with diameters of 10 mm and 15 mm, located at central lateral positions and depths of 10 mm and 28 mm, respectively, was simulated. The transducer settings used for simulation were similar to those of the 128-element linear array L11-5v (Verasonics, Kirkland, WA). The center and sampling frequencies were set to 5.208 MHz and 20.832 MHz, respectively. It should be noted that due to the numerical precision of simulations in Field II, the initial sampling frequency was set to 104.16 MHz, and the simulated data was later downsampled by a factor of 5. All images were simulated using a full synthetic aperture scan, followed by the synthesis of plane-wave images with 384 columns from the acquired data and saved as RF data. We synthesized 100 randomly aberrated versions of each image according to the procedure elaborated in subsection II-B1. Although the non-aberrated version of images was not required for the proposed method, we opted to include them in the published dataset to enhance its comprehensiveness and facilitate the utilization of our data in a broader range of applications. This is because other methods may rely on non-aberrated images as a reference or ground truth. Fig. 2 shows samples from the simulated dataset.

2) *Experimental Phantom*: An L11-5v linear array transducer was operated using a Vantage 256 system (Verasonics, Kirkland, WA) to scan a multi-purpose multi-tissue ultrasound phantom (Model 040GSE, CIRS, Norfolk, VA). We acquired one scan of anechoic cylinders for evaluations and an additional 30 scans from other regions of the phantom for fine-tuning. In each acquisition, 51 single plane-wave images were captured, including one non-aberrated image (not for training and solely for visualization) and 50 randomly aberrated images utilizing pre-generated aberration profiles as elaborated in subsection II-B2. To increase the frame rate, all 1550 required aberration profiles were randomly generated in advance and saved on the disk. Given the fixed position of both the probe and phantom and the sufficiently high frame rate, we assured

that all 51 images belonged to the exact same region.

3) *In-vivo*: An *in-vivo* image acquired from the carotid artery of a volunteer with a cross-sectional view was employed from the publicly available PICMUS dataset [47]. Although this dataset was not explicitly designed for assessing aberration correction techniques, it was utilized due to the unavailability of other *in-vivo* plane-wave images specifically acquired with aberrations as testing on a publicly available dataset allows other researchers to compare to our results.

D. Training

Inspired by Lehtinen *et al.* [48], the U-Net encoder-decoder CNN architecture [49] was employed to map beamformed RF data input to beamformed RF data target output, where both input and target output were distinct randomly aberrated versions of the same realization. The network was trained on 1600 simulated image sets for 5000 epochs, each set comprising 100 aberrated versions. In each epoch, a random pair of aberrated versions were mapped to each other. To optimize memory usage and accelerate the training process, we downsampled images laterally by a factor of 2, resulting in 192 columns for each image. Moreover, normalization was performed by dividing each image by its maximum value, followed by applying the Yeo-Johnson power transformation [50]. The sigmoid function was employed as the activation function of the last layer, and the batch size was 32. We utilized Adam [51] with a zero weight decay as the optimizer. The learning rate was initially set to 10^{-3} and halved at epochs 500, 1000, 1500, and 4000. Fine-tuning on experimental images was performed with the same configurations by extending the training by an additional 20% of the original epochs while utilizing a constant and substantially lower learning rate of 5×10^{-5} . To deal with the attenuation in experimental images, we partitioned images into three axial sections, each with a 3% overlap, and fine-tuned a distinct network for each depth. During testing, we fed each depth of the image to its corresponding network, patched the outputs, and blended the envelope of overlapping margins using weighted averaging before displaying the final image. We implemented the method using PyTorch and trained all the models on two NVIDIA A100 GPUs in parallel.

E. Loss Function

Let $\mathbf{S}, \mathbf{S}', \hat{\mathbf{S}} \in \mathbb{R}^{p \times q}$ represent input aberrated RF data, target output aberrated RF data, and network output, respectively. The aberration-to-aberration problem can be formulated as

$$\hat{\mathbf{S}} = f_{cnn}(\mathbf{S}, \boldsymbol{\theta}), \quad (4)$$

$$\boldsymbol{\theta}^* = \underset{\boldsymbol{\theta}}{\operatorname{argmin}} L(\mathbf{S}', \hat{\mathbf{S}}), \quad (5)$$

where $f_{cnn} : \mathbb{R}^{p \times q} \rightarrow \mathbb{R}^{p \times q}$ is the U-Net, $\boldsymbol{\theta}$ are the network's parameters, and during the training phase, an optimizer is utilized to find optimal parameters $\boldsymbol{\theta}^*$ that minimize the error, measured by a loss function L , between network's output $\hat{\mathbf{S}}$ and target output \mathbf{S}' . In this problem, input and target output were highly fluctuating aberrated RF data, which were randomly substituted at each epoch. We demonstrated in a pilot study in III-A that the network encounters challenges

in mapping pairs when comparing RF data directly using a conventional MSE loss defined as

$$L_{mse}(\mathbf{S}', \hat{\mathbf{S}}) = \frac{1}{p \times q} \|\mathbf{S}' - \hat{\mathbf{S}}\|^2. \quad (6)$$

We showed that utilizing B-mode data in the loss function led to improved network convergence:

$$L_{b-mode}(\mathbf{S}', \hat{\mathbf{S}}) = \frac{1}{p \times q} \|B-mode(\mathbf{S}') - B-mode(\hat{\mathbf{S}})\|^2, \quad (7)$$

where $B-mode(\cdot)$ is the log-compressed envelope data standardized by mean subtraction and division by its standard deviation.

To further improve the network performance, we proposed an adaptively mixed loss function that gradually shifts from B-mode loss to RF loss as the training progresses.

$$L_{adaptive_mixed}(\mathbf{S}', \hat{\mathbf{S}}) = (1 - \alpha)L_{b-mode}(\mathbf{S}', \hat{\mathbf{S}}) + \alpha L_{mse}(\mathbf{S}', \hat{\mathbf{S}}), \quad (8)$$

$$\alpha = \frac{\text{current epoch number}}{\text{total number of epochs}}. \quad (9)$$

Our interpretation is that this loss function guides the optimizer towards a correct solution by initially utilizing simpler data, before gradually incorporating more complex, fluctuating RF data to take full advantage of the richer information, like curriculum learning [52]. This helps to avoid getting stuck in local minima during the initial stages of the optimization.

F. FXPF

Most of the recent aberration correction methods either require multiple plane-wave transmissions [23], [29], or employ multistatic aperture data to synthetically focus at all points [28]. To ensure a fair comparison, we selected the FXPF method, which is applicable to single plane-wave images, and has been utilized for filtering acoustic clutter and random noise [12], and more recently for phase aberration correction [13].

Let us consider the received RF signal at time t by element n located at x_n and denote its Fourier transform as $RF_n(f) = \mathcal{F}\{RF(x_n, t)\}$. The FXPF method establishes an autoregressive model of order d across the channel RF signals received at transducer elements. Specifically, in the frequency domain and for each temporal frequency f_0 , the method predicts a signal as a linear combination of the signals received by the preceding channels:

$$RF_n(f_0) = b_0 RF_{n-1}(f_0) + b_1 RF_{n-2}(f_0) + \dots + b_d RF_{n-p}(f_0). \quad (10)$$

Estimating coefficients b from noisy data filters out non-conforming components based on the established model. Further details can be found in [12], [13]. Although FXPF had been solely employed for focused images, we adapted this method for plane-wave images. The key adjustment involved applying apodization before using the method on the data to avoid image deterioration at shallow depths. This alteration was necessary due to significant variation in channel data across different elements at these depths, where signals from

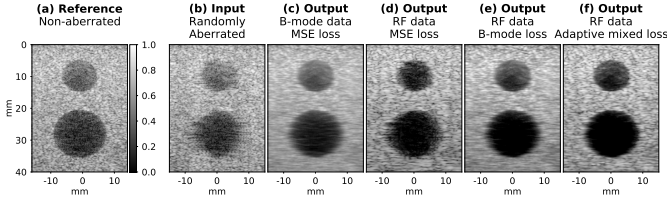


Fig. 3. Training with different data types and loss functions. (a) The non-aberrated image, shown merely as a reference and not used for training. (b) The aberrated input image. The output of the network when it is trained on (c) B-mode data using the MSE loss function, (d) RF data using the MSE loss function, (e) RF data using the MSE of B-mode data as the loss function, and (f) RF data using the adaptive mixed loss function. All images are normalized by their maximum intensity and shown on a 50 dB dynamic range.

more distant elements are irrelevant and negatively affect the autoregressive model.

In all experiments, we employed the FXPF method with an autoregressive model of order 2, stability factor of 0.01, kernel size of one wavelength, and 3 iterations. These settings were chosen because they generated the best results in our cases. As the implementation of this method was not publicly available, we took the initiative to publicly release our own implementation, alongside the other codes used in this study, to enhance the reproducibility of the reported results.

G. Quality Metrics

To quantitatively measure the quality of reconstructed images, we calculated contrast, generalized contrast-to-noise ratio (gCNR) [53], and speckle signal-to-noise ratio (SNR) metrics for the test images:

$$\text{Contrast} = -20 \log_{10}\left(\frac{\mu_t}{\mu_b}\right), \quad (11)$$

$$\text{SNR} = \frac{\mu_b}{\sigma_b}, \quad (12)$$

$$\text{gCNR} = 1 - \int_{-\infty}^{+\infty} \min\{p_t(x), p_b(x)\} dx, \quad (13)$$

where t and b stand for target and background regions, respectively, μ is the mean, and σ is the standard deviation. In (13), x denotes the image value at any given pixel, and $p(x)$ is the probability density function of the values taken by pixels of a region. The gCNR ranges from 0 to 1, with a higher value indicating better contrast. All metrics were calculated on the envelope-detected image in the linear domain before applying the log-compression.

III. RESULTS

A. Toy Pilot Study

To assess the performance of the proposed adaptive mixed loss function, we conducted an isolated toy pilot study merely using the simulated test image described in II-C1. That image consisted of 100 aberrated versions of the same realization, where 99 versions served as a training set, and the remaining one version was used for testing in this pilot study. The network was trained using the configuration specified in Section II-D, in which during each epoch, each of the 99 versions was

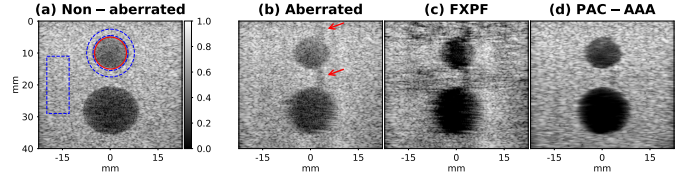


Fig. 4. Simulated test results. (a) The non-aberrated image, shown as a reference and not used for training. (b) The aberrated image reconstructed using DAS. (c) FXPF output. (d) PAC-AAA output. All images are normalized by their maximum intensity and presented on a dynamic range of 50 dB.

randomly mapped to another one. We trained four different networks, fed them with the test version, shown in Fig. 3(b), and compared their outputs. The first network was trained exceptionally using B-mode data as input and output, instead of RF data, with MSE loss. The output is shown in (c), where it is evident that while the cyst boundaries were mostly recovered, the output appears to be blurry compared to the non-aberrated (a) and aberrated (b) images. It is consistent with the findings reported in [54], where the objective was speckle filtering; however, the speckle pattern contains valuable information that can be utilized in applications such as elastography [55]. Motivated by the richer information content of RF data, we retrained the network using RF data, resulting in a sharper output, shown in (d). However, the network encountered challenges in mapping pairs of highly fluctuating aberrated RF data that were randomly substituted at each epoch. Consequently, it encountered challenges in recovering cysts boundaries compared to the B-mode data case.

Inspired by the results from the training with B-mode and RF data, we combined both approaches by retraining the network with RF data as input and output but using MSE of B-mode data as the loss function. As shown in (e), this approach exploited the advantages of the rich information in RF data and produced a sharper image compared to (c) while retaining the ability to recover boundaries more efficiently compared to (d). To further improve the network performance, we employed the proposed adaptive mixed loss function that gradually shifted from B-mode loss to RF loss as the training progressed toward convergence. As shown in (f), this approach maintained the ability to recover boundaries while producing a sharper image compared to (e). Although further investigations are required, we believe that the advantages of the proposed loss function extend beyond the aberration correction task and have the potential to improve the performance of other networks working with RF data in various tasks.

B. Main Study

Based on the findings from the pilot study, we chose the adaptive mixed loss function and utilized it for the subsequent experiments presented in this paper. In the main study, we trained the network using 1600 simulated images and evaluated its performance on 100 aberrated versions of the test image. One such aberrated version, reconstructed using the conventional delay-and-sum (DAS), is shown in Fig. 4(b), followed by the resulting outputs of the FXPF and the proposed method. Note that in contrast to the pilot study, the

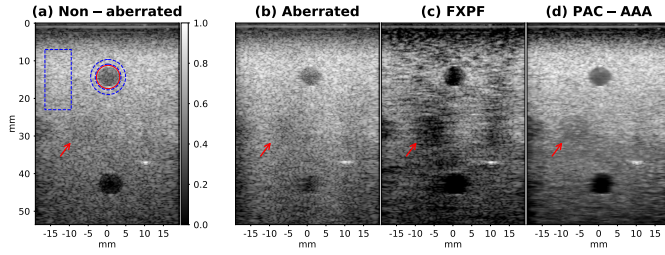


Fig. 5. Experimental phantom results with quasi-physical aberrations. (a) The non-aberrated image, shown merely as a reference, and not used for training. (b) The aberrated image reconstructed using DAS. (c) FXPF output. (d) PAC-AAA output. All images are normalized by their maximum intensity and presented on a dynamic range of 60 dB.

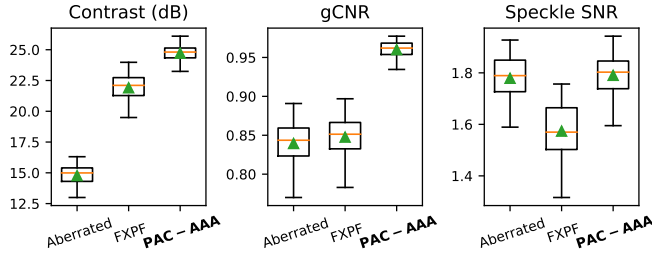


Fig. 6. Contrast (dB), gCNR, and speckle SNR metrics for the aberrated inputs and corrected outputs. Quality metrics were computed over the anechoic cysts at the top and bottom of the simulated test image. The green triangle and orange horizontal line represent the mean and median, respectively.

network, in this case, was trained only on images similar to those depicted in Fig. 2 and had never seen a perfectly circular cyst during the training phase.

To perform a quantitative evaluation, we calculated contrast, gCNR, and speckle SNR for top and bottom anechoic cysts in the test image and reported their mean value. Although target and background regions, used for calculating metrics, were chosen in a similar way for both cysts, they are depicted only for the top cyst in the non-aberrated image in Fig. 4(a) for brevity. For all metrics, the target region was inside a concentric circle with the same radius as that of the cyst (solid red circle). For contrast and gCNR, the background was the region between two concentric circles with radii of 1.1 and 1.5 times the cyst radius (dashed blue circles), while for speckle SNR, it was inside a rectangle far from the cyst (dashed blue rectangle). The results were obtained by averaging across 100 aberrated versions of the test image and are shown in Fig. 6, where the exact numbers are reported in Table I.

Fig. 5 presents the results for one of the aberrated versions of the experimental phantom test image, which was acquired with quasi-physical aberrations. It is evident that the proposed method compensated for the aberration effect without introducing unwanted artifacts to the image. Similar to the

TABLE I
QUALITY METRICS FOR THE SIMULATED TEST IMAGE ($\mu \pm \sigma$).

Metric	DAS	FXPF	PAC-AAA
Contrast (dB)	14.77 \pm 0.96	21.91 \pm 1.23	24.72 \pm 0.61
gCNR	0.84 \pm 0.03	0.85 \pm 0.03	0.96 \pm 0.01
Speckle SNR	1.78 \pm 0.08	1.57 \pm 0.10	1.79 \pm 0.08

TABLE II
QUALITY METRICS FOR THE EXPERIMENTAL PHANTOM WITH QUASI-PHYSICAL ABERRATION ($\mu \pm \sigma$).

Metric	DAS	FXPF	PAC-AAA
Contrast (dB)	9.48 \pm 1.24	11.59 \pm 1.44	12.22 \pm 0.44
gCNR	0.73 \pm 0.05	0.69 \pm 0.08	0.87 \pm 0.01
Speckle SNR	1.61 \pm 0.03	1.13 \pm 0.11	1.62 \pm 0.04

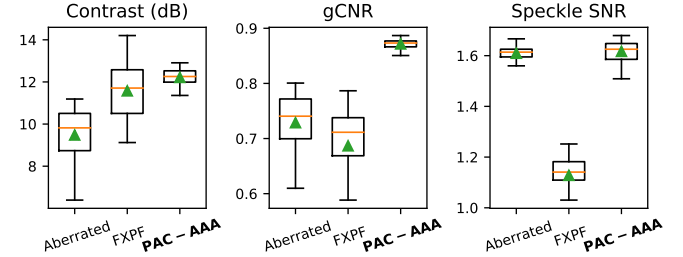


Fig. 7. Contrast (dB), gCNR, and speckle SNR metrics for the aberrated inputs and corrected outputs. Quality metrics were computed over the anechoic cysts at the top and bottom of the test image from the experimental phantom with quasi-physical aberration. The green triangle and orange horizontal line represent the mean and median, respectively.

simulated test image, the mean quality metrics for the top and bottom anechoic cysts were calculated, averaged over all 50 aberrated versions, and presented in Fig. 7 and Table II.

Fig. 8 presents the results for the experimental phantom aberrated with a physical aberrator. The first column displays the image reconstructed using conventional DAS, while the second and third columns show the corrected images using FXPF and proposed methods, respectively. To enhance visual comparability, the top and bottom cysts were cropped and displayed under their corresponding images, where each horizontal line of the cropped images was normalized to its maximum intensity. The results indicate that the proposed method outperformed the others in accurately recovering cyst boundaries, especially the bottom one. Finally, we applied both

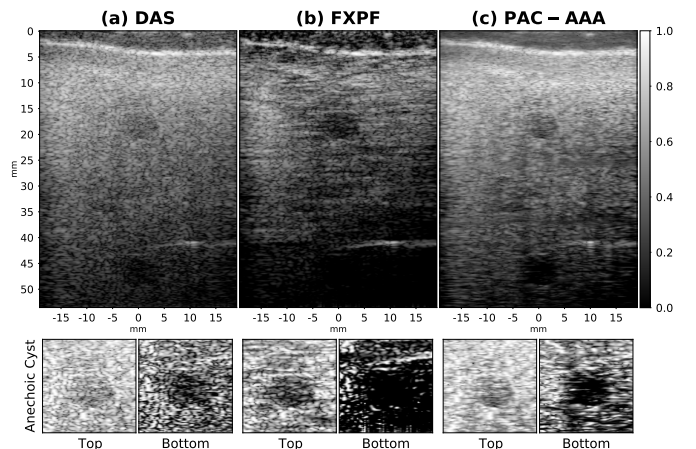


Fig. 8. Experimental phantom aberrated with a physical aberrator layer. (a) DAS reconstruction. (b) Correction with FXPF. (c) PAC-AAA output. All images are shown on a 60 dB dynamic range. Images in the first row are normalized by their global maximum intensity. In the second row, each horizontal line of the cropped region of interest was normalized to its maximum intensity to enhance visual comparability.

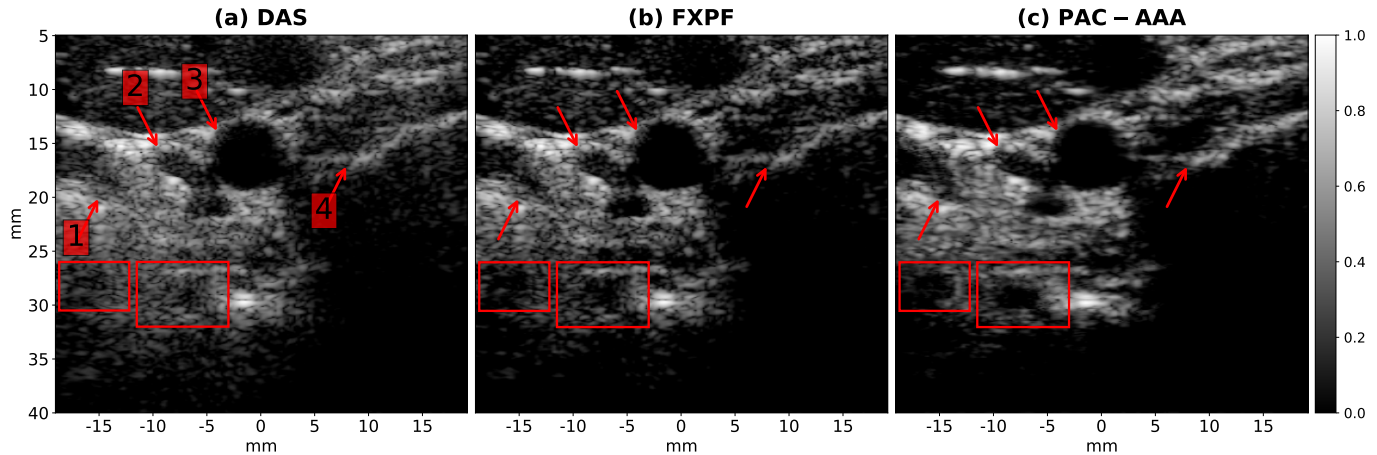


Fig. 9. *In-vivo* carotid artery cross-section image from the PICMUS dataset. (a) DAS reconstruction. (b) Correction with FXPF. (c) PAC-AAA output. All images are normalized by their maximum intensity and shown on a 50 dB dynamic range.

the FXPF and the proposed PAC-AAA method to the *in-vivo* carotid artery cross-section image from the PICMUS dataset and showed the results in Fig. 9. The longitudinal view results are presented in the Supplementary Video (also available from <http://code.sonography.ai/pac-aaa>).

IV. DISCUSSION

In the pilot study, we conducted an experiment where we mapped different aberrated versions of the same image to each other to demonstrate the effectiveness of the proposed adaptive mixed loss function in correcting the phase aberration effect without over-smoothing the RF data and without requiring a non-aberrated ground truth. Notably, the results of this experiment also revealed an interesting finding. Specifically, it is evident in Fig. 3 that not only the phase aberration effect introduced in the input (b) is corrected in the output (f), but a higher contrast is achieved even compared to the non-aberrated reference image (a). According to our interpretation, one possible explanation for this superior performance may be attributed to the ability of the network to fully exploit the RF data across the entire image in order to output the corrected version, where it can leverage the matched patterns learned from one part of the image, such as the top cyst, to correct another part, such as the bottom cyst. This can be analogized to the non-local means denoising algorithm [56] in traditional image processing, which has been shown to outperform local mean filters in achieving higher performance. As a result, the network does not solely rely on RF data from local areas to correct the aberration but instead takes advantage of information from the entire image, resulting in an improved image even compared to the reference image. Another possible explanation is that the network develops ability to effectively eliminate noise and clutter while randomly mapping one aberrated version to another. Since the noise and clutter vary across different aberrated versions, the network learns to disregard them during image reconstruction, resulting in an improved output compared to the reference image. Interestingly, this finding aligns with the study by Jing *et al.* [57], in which they proposed enhancing the spatial resolution of plane-wave

images by introducing weak aberration into received data. They calculated the pixel-wise standard deviation of multiple aberrated versions and subtracted the result from the original image. Although our approach differs entirely from theirs, the concept of obtaining an enhanced image from its aberrated versions is similar and can explain the improvement over the reference image.

The main study involved training a general model on a dataset containing images similar to those presented in Fig. 2 and evaluating its performance using the test image depicted in Fig. 4. Red arrows in the aberrated image (b) highlight the shadowing effect resulting from the perturbed wavefront during transmission. The proposed method outperformed FXPF, which failed to detect and correct this effect due to its reliance solely on local signal information of a single image. As previously mentioned, the FXPF method eliminates components that do not conform to the autoregressive model across the echo signals received at the transducer elements. Nevertheless, in cases where all the echo signals experience a decrease in amplitude, the algorithm is unable to estimate a corrected signal with a higher amplitude. Instead, it tends to amplify the darkness of already dark regions, which may not necessarily correspond to anatomically relevant tissues, such as an anechoic cyst. The findings are consistent with the metrics reported in Table I, indicating that while the FXPF algorithm improved contrast, it had a slight impact on gCNR. Conversely, the proposed PAC-AAA method not only enhanced contrast but also achieved a higher gCNR of 0.96, which is substantially closer to the maximum value of 1.

Similarly, we can see in Fig. 5 that the proposed method recovered the size of the anechoic cyst at the bottom of the image more accurately, in contrast to the FXPF method that resulted in an overestimation of its size. As reported in Table II, although the FXPF method improved the mean contrast of cysts, the mean gCNR actually decreased due to its aforementioned limitation. Conversely, the proposed method consistently improved both the contrast and gCNR metrics. In addition to the top and bottom anechoic cysts, this image contained four grayscale targets positioned at a depth of 30

mm and arranged from left to right with contrast levels of -6 dB, -3 dB, +3 dB, and +6 dB relative to the background. It is evident that the target indicated with the red arrow was recovered with higher accuracy in terms of both its shape and its contrast level, aligned with our prior knowledge that it was a hypoechoic cyst with a contrast level of -3 dB.

In both the simulation and experimental phantoms with quasi-physical experiments, the FXPF method reduced the speckle SNR. As demonstrated in Figs. 4 and 5, this method increased the variance of the values within the blue rectangle while it preserved or even reduced their mean (darker region). Thus, an increase in speckle SNR was inevitable. In contrast, the proposed method consistently maintained speckle SNR comparable to that of the aberrated image reconstructed using the conventional DAS method. We consider this maintenance of speckle SNR a positive outcome because networks have a tendency to smooth B-mode images by averaging across matched patterns. One of the objectives of proposing the adaptive mixed loss function was to prevent the network from oversmoothing B-mode images. While smoothing the speckle pattern may result in an increase in the speckle SNR, preserving it was a desirable goal of the proposed method.

Fig. 8 shows a similar trend as observed in Figs. 4 and 5, where the improvement in the bottom cyst is more prominent than in the top cyst. This observation can be attributed to the fact that the severity of the phase aberration effect, which needs to be corrected, is lower at shallower depths compared to deeper depths for two reasons. Firstly, perturbations in the wavefront escalate with propagation, leading to an increase in the aberration effect during transmission as the wavefront moves forward. Secondly, in plane-wave imaging, the reconstruction process uses a smaller aperture size a at shallower depths and gradually increases it for deeper depths according to the F-number. This reduces the problem of incoherent summation at low depths, as only a lower number of neighbor elements are involved in image reconstruction.

In Fig. 9, we compared different methods on an *in-vivo* cross-sectional image of the carotid artery obtained from the PICMUS dataset. Despite the absence of intentional aberrations and any ground truth, we observed interesting results in this image. Several parts of the image were modified after applying the aberration correction methods, and we highlighted some of the notable alterations. In the case of the right subclavian vein (arrow #1), the reconstructed image obtained by the DAS method exhibited indistinct and blurry boundaries. Although the FXPF method mitigated the issue, the proposed PAC-AAA method achieved the highest level of boundary sharpness, allowing differentiation of the vessel wall and its anechoic lumen. A similar trend was observed for the right jugular vein (arrow #2) and right common carotid artery (arrow #3), wherein the proposed method reconstructed images with superior tissue differentiation as evidenced by sharper boundaries and more distinct anatomical structures compared to other methods. Similarly, the proposed method demonstrated the sharpest posterior edge for the right thyroid lobe (arrow #4), thereby further improving the visual quality of the reconstructed image. Additionally, the PAC-AAA method revealed ovoid-shaped structures within the two

rectangles, which may represent the right subclavian artery (small rectangle) and right vertebral artery (large rectangle) seen cross-sectionally. These areas are barely visible using the DAS method, potentially because of their depth and size, as well as potential aberration induced by the highly anisotropic sternocleidomastoid muscle (the large oval at the top left of the figure). Although an aberration-free ground truth for this image is unavailable, this representation is supported by the similarity of the pattern within these rectangles in the DAS image to the aberrated anechoic cysts seen in the phantom images and the fact that both the FXPF (which is not a learning-based method) and the proposed method detected them by attempting to enhance their contrast, while the proposed method produced substantially sharper boundaries for these tissues.

The capability of a network trained based on the near-field phase screen model to correct phase aberration in an image, such as the presented *in-vivo* image at the level of the carotid artery, which might be affected by distributed aberrations and does not necessarily adhere to the model, could be a subject of doubt. To address this concern, we can assume that the aberration at any given point within a medium is a consequence of variations in sound speed along the trajectory linking said point to each element of the aperture. Thus, regardless of the distribution of the aberrator, the variations in sound speed that contribute to the aberration of a particular point can still be approximated by a near-field phase screen. In other words, distributed aberrations throughout a heterogeneous medium can be characterized by multiple aberration profiles, each corresponding to a specific point. Chau *et al.* [14] developed a locally adaptive phase aberration correction method based on this assumption, estimating a local aberration profile at each point in the discretized image domain. While theoretically, each point may require a dedicated aberration profile, in practice, we believe that a single aberration profile may be sufficient to model the aberration induced at adjacent points, dramatically reducing the number of required profiles to characterize a distributed aberration. Although this assumption requires further investigations in future work, we speculate that a network trained and fine-tuned on over 160,000 unique aberration profiles can learn from presented variations and become capable of correcting more complex aberrations locally, even if they cannot be modeled by a single near-field phase screen.

V. CONCLUSIONS

We proposed a new DL-based approach for correcting phase aberration that eliminates the requirement for ground truths. We illustrated that a conventional loss function, such as MSE, is inadequate to achieve optimal performance and introduced an adaptive mixed loss function to train a network capable of mapping aberrated RF data to aberrated RF data. This approach permits training or fine-tuning using experimental images without prior assumptions about the presence or absence of aberration. Furthermore, we demonstrated the feasibility of obtaining required data for this method using a programmable transducer and acquiring multiple aberrated versions of the same scene during a single scan. Furthermore,

apart from releasing the code for the proposed and the FXPF method, we will also make available to the public a dataset containing more than a thousand sets of single plane-wave images stored as RF data, where each set comprises 100 aberrated versions of the same realization, as well as the non-aberrated version, aiming to facilitate the advancement of DL-based methods for correcting phase aberration in ultrasound images.

REFERENCES

- [1] N. Masoumi *et al.*, “The big bang of deep learning in ultrasound-guided surgery: a review,” *IEEE TUFFC*, 2023.
- [2] G. F. Pinton, G. E. Trahey, and J. J. Dahl, “Sources of image degradation in fundamental and harmonic ultrasound imaging using nonlinear, full-wave simulations,” *IEEE TUFFC*, apr 2011.
- [3] S. Flax and M. O’Donnell, “Phase-aberration correction using signals from point reflectors and diffuse scatterers: basic principles,” *IEEE TUFFC*, nov 1988.
- [4] S. A. Goss, R. L. Johnston, and F. Dunn, “Compilation of empirical ultrasonic properties of mammalian tissues. II,” *The Journal of the Acoustical Society of America*, jul 1980.
- [5] M. A. O’Reilly and K. Hynynen, “A super-resolution ultrasound method for brain vascular mapping,” *Medical Physics*, oct 2013.
- [6] S. A. Goss, R. L. Johnston, and F. Dunn, “Comprehensive compilation of empirical ultrasonic properties of mammalian tissues,” *The Journal of the Acoustical Society of America*, aug 1978.
- [7] M. Karaman *et al.*, “A phase aberration correction method for ultrasound imaging,” *IEEE TUFFC*, jul 1993.
- [8] L. Nock, G. E. Trahey, and S. W. Smith, “Phase aberration correction in medical ultrasound using speckle brightness as a quality factor,” *The Journal of the Acoustical Society of America*, may 1989.
- [9] B.-F. Osmanski *et al.*, “Aberration correction by time reversal of moving speckle noise,” *IEEE TUFFC*, jul 2012.
- [10] Pai-Chi Li and Meng-Lin Li, “Adaptive imaging using the generalized coherence factor,” *IEEE TUFFC*, feb 2003.
- [11] D. Napolitano *et al.*, “Sound speed correction in ultrasound imaging,” *Ultrasonics*, dec 2006.
- [12] J. Shin and L. Huang, “Spatial Prediction Filtering of Acoustic Clutter and Random Noise in Medical Ultrasound Imaging,” *IEEE TMI* 2017.
- [13] J. Shin, L. Huang, and J. T. Yen, “Spatial Prediction Filtering for Medical Ultrasound in Aberration and Random Noise,” *TUFFC*, 2018.
- [14] G. Chau *et al.*, “A Locally Adaptive Phase Aberration Correction (LAPAC) Method for Synthetic Aperture Sequences,” *Ultrasonic Imaging*, jan 2019.
- [15] W. Lambert *et al.*, “Distortion matrix approach for ultrasound imaging of random scattering media,” *Proceedings of the National Academy of Sciences*, jun 2020.
- [16] W. Lambert *et al.*, “Ultrasound Matrix Imaging—Part I: The Focused Reflection Matrix, the F-Factor and the Role of Multiple Scattering,” *IEEE TMI*, dec 2022.
- [17] W. Lambert *et al.*, “Ultrasound Matrix Imaging—Part II: The Distortion Matrix for Aberration Correction Over Multiple Isoplanatic Patches,” *IEEE TMI*, dec 2022.
- [18] S. J. Sanabria *et al.*, “Spatial domain reconstruction for imaging speed-of-sound with pulse-echo ultrasound: simulation and in vivo study,” *Physics in Medicine and Biology*, oct 2018.
- [19] R. Rau *et al.*, “Ultrasound Aberration Correction based on Local Speed-of-Sound Map Estimation,” in *2019 IEEE IUS*.
- [20] M. Jaeger *et al.*, “Full correction for spatially distributed speed-of-sound in echo ultrasound based on measuring aberration delays via transmit beam steering,” *Physics in Medicine and Biology*, jun 2015.
- [21] R. Ali and J. J. Dahl, “Distributed Phase Aberration Correction Techniques Based on Local Sound Speed Estimates,” *2018 IEEE IUS*.
- [22] J. A. Sethian and A. M. Popovici, “3-D travelttime computation using the fast marching method,” *GEOPHYSICS*, mar 1999.
- [23] P. Stähli *et al.*, “Improved forward model for quantitative pulse-echo speed-of-sound imaging,” *Ultrasonics*, dec 2020.
- [24] M. Jakovljevic *et al.*, “Local speed of sound estimation in tissue using pulse-echo ultrasound: Model-based approach,” *The Journal of the Acoustical Society of America*, 2018.
- [25] M. E. Anderson and G. E. Trahey, “The direct estimation of sound speed using pulse-echo ultrasound,” *The Journal of the Acoustical Society of America*, nov 1998.
- [26] R. Ali and J. J. Dahl, “Travel-Time Tomography for Local Sound Speed Reconstruction Using Average Sound Speeds,” *2019 IEEE IUS*.
- [27] T. Brevett *et al.*, “Speed of Sound Estimation at Multiple Angles from Common Midpoint Gathers of Non-Beamformed Data,” *2022 IEEE IUS*.
- [28] R. Ali *et al.*, “Distributed Aberration Correction Techniques Based on Tomographic Sound Speed Estimates,” *IEEE TUFFC*, may 2022.
- [29] H. Bendjador, T. Deffieux, and M. Tanter, “The SVD Beamformer: Physical Principles and Application to Ultrafast Adaptive Ultrasound,” *IEEE TMI*, oct 2020.
- [30] M. Sharifzadeh, H. Benali, and H. Rivaz, “Phase Aberration Correction: A Convolutional Neural Network Approach,” *IEEE Access*, 2020.
- [31] M. Feigin, D. Freedman, and B. W. Anthony, “A Deep Learning Framework for Single-Sided Sound Speed Inversion in Medical Ultrasound,” *IEEE TBME*, apr 2020.
- [32] F. Khun Jush, P. M. Dueppenbecker, and A. Maier, “Data-Driven Speed-of-Sound Reconstruction for Medical Ultrasound: Impacts of Training Data Format and Imperfections on Convergence,” 2021.
- [33] F. K. Jush *et al.*, “DNN-based Speed-of-Sound Reconstruction for Automated Breast Ultrasound,” in *2020 IEEE IUS*.
- [34] J. R. Young *et al.*, “SoundAI: Improved Imaging with Learned Sound Speed Maps,” in *2022 IEEE IUS*.
- [35] T. Koike *et al.*, “Deep learning for hetero-homo conversion in channel-domain for phase aberration correction in ultrasound imaging,” *Ultrasonics*, mar 2023.
- [36] W.-H. Shen and M.-L. Li, “A Novel Adaptive Imaging Technique Using Point Spread Function Reshaping,” in *2022 IEEE IUS*.
- [37] A. C. Luchies and B. C. Byram, “Assessing the Robustness of Frequency-Domain Ultrasound Beamforming Using Deep Neural Networks,” *IEEE TUFFC*, nov 2020.
- [38] S. Khan, J. Huh, and J. C. Ye, “Phase Aberration Robust Beamformer for Planewave US Using Self-Supervised Learning,” 2022. arXiv:2202.08262
- [39] M. Sharifzadeh, H. Benali, and H. Rivaz, “Phase Aberration Correction without Reference Data: An Adaptive Mixed Loss Deep Learning Approach,” mar 2023. arXiv:2303.05747
- [40] T. Bancel *et al.*, “Comparison Between Ray-Tracing and Full-Wave Simulation for Transcranial Ultrasound Focusing on a Clinical System Using the Transfer Matrix Formalism,” *IEEE TUFFC*, jul 2021.
- [41] J. Dahl, D. Guenther, and G. Trahey, “Adaptive imaging and spatial compounding in the presence of aberration,” *IEEE TUFFC*, jul 2005.
- [42] L. M. Hinkelman, *et al.*, “Measurement and correction of ultrasonic pulse distortion produced by the human breast,” *The Journal of the Acoustical Society of America*, mar 1995.
- [43] A. Fernandez *et al.*, “Aberration measurement and correction with a high resolution 1.75D array,” in *2001 IEEE Ultrasonics Symposium. Proceedings. An International Symposium*.
- [44] J. A. Jensen, “FIELD: A program for simulating ultrasound systems,” *Medical and Biological Engineering and Computing*, 1996.
- [45] C. Xia *et al.*, “What is and What is Not a Salient Object? Learning Salient Object Detector by Ensembling Linear Exemplar Regressors,” in *IEEE CVPR*, jul 2017.
- [46] D. Hyun *et al.*, “Beamforming and speckle reduction using neural networks,” *IEEE TUFFC*, 2019.
- [47] H. Liebgott *et al.*, “Plane-Wave Imaging Challenge in Medical Ultrasound,” in *2016 IEEE IUS*.
- [48] J. Lehtinen *et al.*, “Noise2Noise: Learning Image Restoration without Clean Data,” *35th ICML*, mar 2018.
- [49] O. Ronneberger, P. Fischer, and T. Brox, “U-net: Convolutional networks for biomedical image segmentation,” in *MICCAI*, may 2015.
- [50] I.-K. Yeo, “A new family of power transformations to improve normality or symmetry,” *Biometrika*, dec 2000.
- [51] D. P. Kingma and J. L. Ba, “Adam: A method for stochastic optimization,” in *3rd ICLR*, 2015.
- [52] Y. Bengio *et al.*, “Curriculum learning,” in *ACM International Conference Proceeding Series*, jun 2009.
- [53] A. Rodriguez-Molares *et al.*, “The Generalized Contrast-to-Noise Ratio: A Formal Definition for Lesion Detectability,” *IEEE TUFFC*, 2020.
- [54] R. Göbl, C. Hennersperger, and N. Navab, “Speckle2Speckle: Unsupervised Learning of Ultrasound Speckle Filtering Without Clean Data,” jul 2022. arXiv:2208.00402
- [55] A. K. Z. Tehrani *et al.*, “Bi-Directional Semi-Supervised Training of Convolutional Neural Networks for Ultrasound Elastography Displacement Estimation,” *IEEE TUFFC*, apr 2022.
- [56] A. Buades, B. Coll, and J.-M. Morel, “A Non-Local Algorithm for Image Denoising,” in *IEEE CVPR*, 2005.
- [57] B. Jing and B. D. Lindsey, “Phase modulation beamforming for ultrafast plane wave imaging,” *IEEE TUFFC*, 2020.